Photoacoustics 29 (2023) 100444

Contents lists available at ScienceDirect

Photoacoustics

journal homepage: www.elsevier.com/locate/pacs

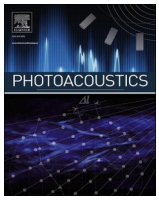

Three-dimensional non-invasive brain imaging of ischemic stroke by integrated photoacoustic, ultrasound and angiographic tomography (PAUSAT)

Luca Menozzi [a,1], Ángela del Águila [b,1], Tri Vu [a], Chenshuo Ma [a], Wei Yang [b,*], Junjie Yao [a,*]

[a] Department of Biomedical Engineering, Duke University, Durham 27708, NC, USA
[b] Multidisciplinary Brain Protection Program, Department of Anesthesiology, Duke University School of Medicine, Durham 27710, NC, USA

ARTICLE INFO

Keywords:
Photoacoustic imaging
Photoacoustic tomography
Acoustic angiography
Ischemic stroke
Hemodynamics
Blood oxygenation
Blood perfusion
Microbubbles

ABSTRACT

We present an ischemic stroke study using our newly-developed PAUSAT system that integrates photoacoustic computed tomography (PACT), high-frequency ultrasound imaging, and acoustic angiographic tomography. PAUSAT is capable of three-dimensional (3D) imaging of the brain morphology, blood perfusion, and blood oxygenation. Using PAUSAT, we studied the hemodynamic changes in the whole mouse brain induced by two common ischemic stroke models: the permanent middle cerebral artery occlusion (pMCAO) model and the photothrombotic (PT) model. We imaged the same mouse brains before and after stroke, and quantitatively compared the two stroke models. We observed clear hemodynamic changes after ischemic stroke, including reduced blood perfusion and oxygenation. Such changes were spatially heterogenous. We also quantified the tissue infarct volume in both stroke models. The PAUSAT measurements were validated by laser speckle imaging and histology. Our results have collectively demonstrated that PAUSAT can be a valuable tool for non-invasive longitudinal studies of neurological diseases at the whole-brain scale.

1. Introduction

Stroke is a common and devastating disease that affects millions of people in the US. There are two main types of stroke: ~87 % of strokes are ischemic (vessel blockage), while the rest are hemorrhagic (bleeding) in nature [1–3]. Current effective treatment for ischemic stroke is limited to reperfusion therapy. This therapy, however, is constrained by strict selection criteria of patients, and thus, is not applicable to the majority of ischemic stroke patients. As such, many stroke survivors have permanent vessel occlusion. During the last decades, tremendous efforts have been invested into experimental stroke research. Disappointingly, we still do not have much to offer for stroke patients and the search for new stroke therapies continues. Additionally, it has been described that COVID-19 may increase the likelihood of stroke and stroke severity, highlighting even more the importance of the continuous study of stroke [4–6].

Evaluation of novel therapeutic strategies in ischemic stroke normally involves histological analysis and behavioral testing on animal models, together providing essential information to determine treatment outcomes. One key quantitative readout is infarct volume in the brain tissue, which is commonly measured using triphenyltetrazolium chloride (TTC) staining. However, this post-mortem analysis only reveals information on end-point state of stroke recovery. Although small-animal MRI is capable of longitudinally monitoring stroke infarcts, it is cost prohibitive. Behavioral tests can be performed at multiple time-points and indirectly indicate severity of brain damage, but they provide no concrete physiological or anatomical information. Therefore, there is still a need for technologies that can provide cost-effective, non-invasive, longitudinal evaluation of the stroke severity on small animal models.

In this study, we aim to apply a new small-animal imaging technology to stroke studies that can provide complimentary information. Photoacoustic tomography (PAT) is a hybrid imaging modality that uses short pulse laser light to induce deep-penetrating acoustic waves inside biological tissues, via the photoacoustic effect [7,8]. Due to the strong optical absorption of oxyhemoglobin (HbO_2) and deoxyhemoglobin (HbR) [9], PAT can provide structural information of blood vessels and functional information of blood oxygenation, without the use of

* Corresponding authors.
E-mail addresses: wei.yang@duke.edu (W. Yang), junjie.yao@duke.edu (J. Yao).
[1] These authors contributed equally

https://doi.org/10.1016/j.pacs.2022.100444
Received 13 July 2022; Received in revised form 9 October 2022; Accepted 23 December 2022
Available online 25 December 2022

exogenous contrast agents. Thus, PAT is a promising tool for studying the brain's hemodynamics in small-animal stroke models, particularly by providing blood oxygenation measurement. Blood oxygenation is an important functional parameter that can be used for evaluating stroke at both acute and chronic stages [10,11]. At the acute stage, blood oxygenation can reflect the stroke-induced vessel impairment and tissue hypoxia. At the chronic stage, blood oxygenation can indicate the progress of tissue restoration. There are two major implementations of PAT: photoacoustic microscopy (PAM) and photoacoustic computed tomography (PACT) [12]. PAM can achieve high-resolution imaging of blood vessels but is limited in the imaging depth to several millimeters. On the other hand, PACT can image several centimeters deep in tissue but has lower spatial resolution than PAM. PACT is better suited for non-invasive brain imaging; however, it is limited by its poor spatial resolution.

Acoustic angiography (AA) is a contrast-enhanced ultrasound imaging method that can map blood perfusion [13]. Microbubbles (MBs), such as perfluorocarbon gases enclosed by lipid shells, can be injected into the bloodstream and enhance acoustic contrast of blood vessels due to their nonlinear response to low-frequency ultrasound waves (e.g., 2 MHz), and their acoustic impedance mismatch with the surrounding tissue [14]. MBs produce a broadband response when excited at their resonant frequency, including subharmonic and super harmonic signals. The tissues generally produce weak super harmonic response. This enables the acoustic echo signals originated from MBs to be separated from the signals originated from the tissues. In AA, a dual-element (or dual-frequency) transducer transmits low-frequency ultrasound waves and receives high-frequency ultrasound waves to allow automatic separation of MBs and tissues without the need of post-imaging processing [15]. AA can produce high-resolution images of blood vessel perfusion. However, AA lacks information on the functional status of the vessels such as blood oxygenation. Thus, taking advantage of the complementary imaging contrast of PACT and AA, we have recently developed a new PAUSAT imaging system that integrates PACT, AA, and high-frequency B-mode ultrasound imaging, simultaneously providing morphological, functional, and molecular imaging on the same animals [16].

This study applies PAUSAT in preclinical ischemic stroke studies using two different models. We first introduce the imaging principle of the PAUSAT system, followed by a detailed description of the stroke animal models. We then present co-registered brain images before and after ischemic stroke, and we show the anatomical and functional impacts of ischemic stroke as imaged by PAUSAT. The PAUSAT results were validated by laser speckle imaging and histology. We conclude the paper by discussing the limitations and future improvements of our technology for stroke studies.

2. Materials and methods

2.1. Imaging principle of PAUSAT system

The PAUSAT system (Fig. 1) was adapted from the Vega robotic imaging system (SonoVol, Inc., Durham, NC). PAUSAT consists of a dual-element wobbler ultrasound transducer and a linear-array ultrasound transducer, both mounted on the same motorized platform (Fig. 1 (b)). PAUSAT uses two separate transducers to address the differing requirements for AA and PACT. AA requires a low-frequency transmitting element to achieve a high mechanical index (MI), which is necessary for generating strong super harmonic signals by the microbubbles. A high-frequency receiving element is necessary to detect the super harmonic signals. On the other hand, PACT requires a transducer array, rather than a single element, to achieve parallel signal detection and high imaging speed. Furthermore, a low detection frequency is necessary in PACT to detect laser-induced ultrasound waves originating from the deep brain. The motorized platform and transducers are submerged in a hydrocarbon fluid, with an optically and acoustically

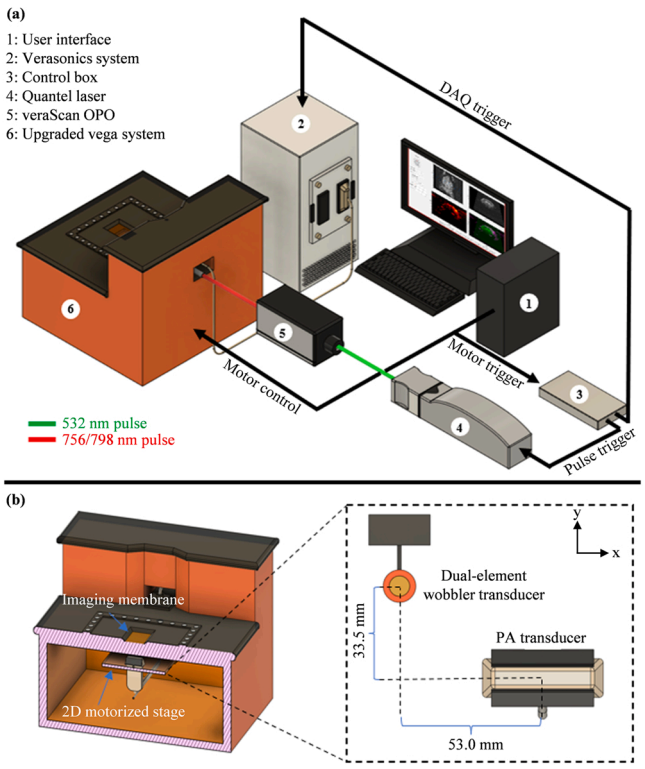

Fig. 1. The imaging principle of PAUSAT. (a) Overall schematic of the PAUSAT system. (b) The inside view of the PAUSAT system, including a dual-element wobbler transducer for B-mode ultrasound (US) and AA, and a linear array transducer with bilateral laser excitation for PACT. Both transducers are mounted on the same motorized stage with a fixed distance. The linear array transducer is mounted 6 mm below the dual-element wobbler along the z-axis to compensate for their different focal depths (25 mm and 19 mm, respectively).

transparent membrane window through which images are acquired. The mounting of both transducers on the same motorized platform allows for 3D scan acquisitions, in which the transducers are automatically moved along the scanning direction in discrete steps, acquiring 2D images in the lateral and axial plane at each elevational step. The dual-element wobbler transducer is made of a low-frequency transmitting element centered at ~2 MHz and a high-frequency receiving element centered at ~26 MHz. The pulse repetition frequency is ~1 kHz with 256 A-lines acquired per frame, and a frame rate of ~4 Hz. The two elements are concentrically aligned and share a 19 mm focal depth. In the AA mode, the outer (low-frequency) element bursts the MBs at their resonant frequency and the inner (high-frequency) element receives the super harmonic signals of the MBs. The peak negative pressure of the transmit pulse in the AA mode is ~1 MPa with a corresponding MI of ~0.707. The inner element of the wobbler transducer is also capable of high-frequency B-mode US imaging, with a frequency range of 10–50 MHz. Both 3D B-mode US and AA volumes are generated using a pixel-based volume reconstruction algorithm (PLUS Toolkit) [17]. The linear-array transducer consists of 128 elements centered at 5 MHz (L7–4, Philips, USA), and is bilaterally coupled with optical fiber bundles in a line configuration along the transducer. The light source for PACT is an Nd:YAG laser (Q-smart 850, Quantel Laser, USA) that can emit at 532 nm with a pulse repetition rate of 10 Hz. The 532 nm light is used to pump an optical parametric oscillator (OPO) (veraScan-L532, Spectral Physics, USA) to generate light ranging from 680 nm to 900 nm (Fig. 1(a)). The output pulse from the OPO is directed into a fiber optic cable that bifurcates to provide illumination for PACT. The PA data is acquired by a programmable ultrasound scanner (Vantage 256, Verasonics, USA). A control box with an FPGA (myRIO, National Instruments, USA) is

programmed to synchronize the motorized stage motion, laser firing, and PA data acquisition. 2D PACT images are generated using a dual speed-of-sound delay-and-sum reconstruction method [16]. Stacks of 2D PA images are then combined to create a 3D PACT volume.

2.2. Stroke mouse models

2.2.1. Animals

Male and female C57Bl/6 mice (2–6 months old, Jackson Lab) were used for these studies. All animal procedures were approved by the Duke University Medical Center Animal Care and Use Committee and were conducted in accordance with the United States Public Health Service's Policy on Humane Care and Use of Laboratory Animals.

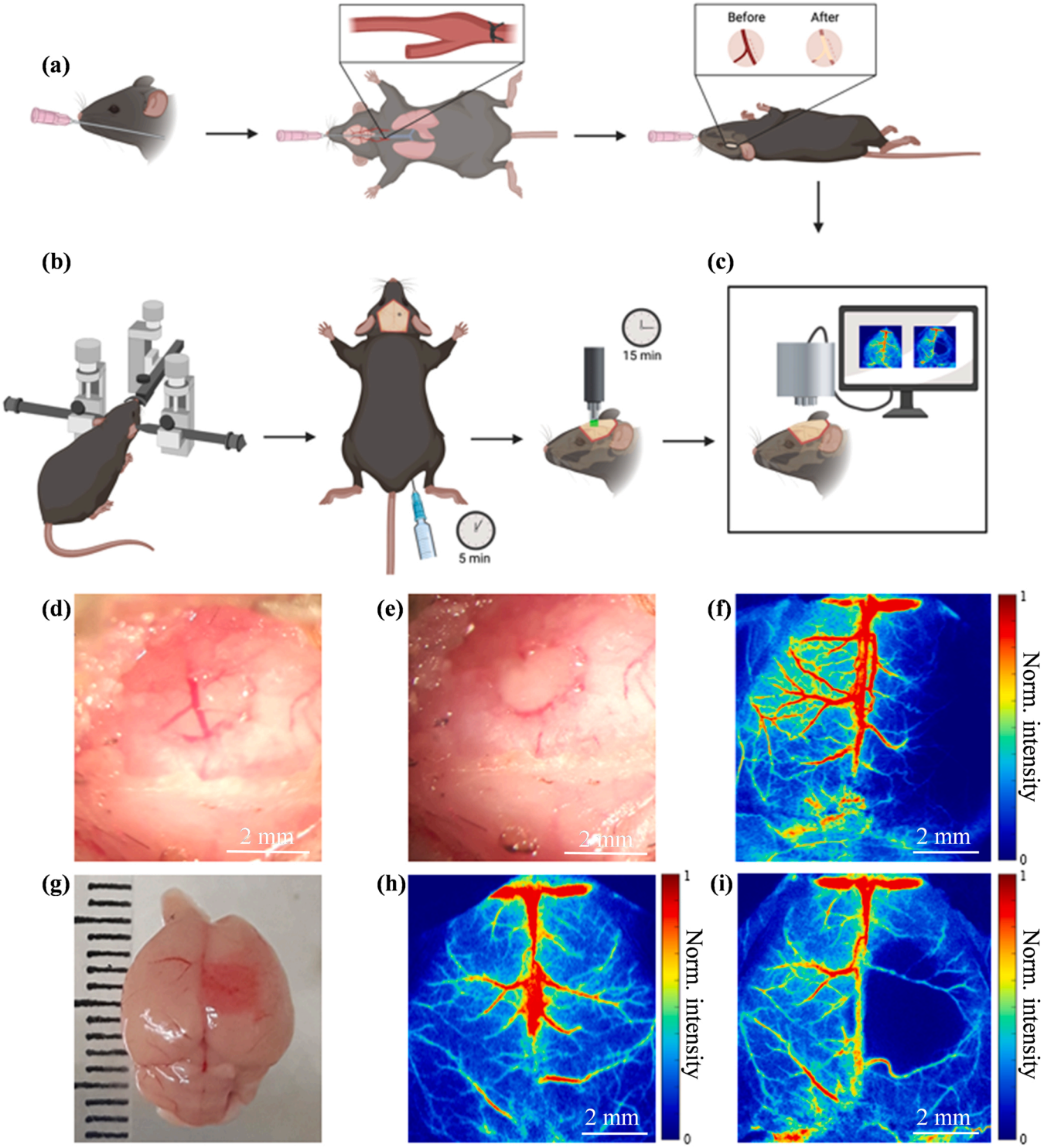

Fig. 2. pMCAO and PT stroke models. (a) Illustration of the surgical procedure for pMCAO. (b) Illustration of the surgical procedure for PT stroke (created with Biorender.com). (c) Setup for laser speckle contrast imaging (LSCI). (d) Photo of the MCA before cauterization. (e) Photo of the MCA after cauterization. (f) Example LSCI 3 days after pMCAO. (g) Photo of the brain 1 day after PT stroke. (h) Example LSCI of an uninjured brain before PT. (i) Example LSCI 1 day after PT stroke.

2.2.2. Permanent middle cerebral artery occlusion (pMCAO)

We modified our transient MCAO model [18]. Mice were anesthetized, intubated using a 20-gauge IC catheter, and maintained with 1.5 % isoflurane in 30 % oxygen and 70 % nitrogen throughout the procedure. The rectal temperature was maintained at 37.0 ± 0.5 °C using a heat lamp. A midline neck incision was made, and the right common carotid artery (CCA) was exposed and ligated using 4.0 silk suture. A small incision was made between the right eye and ear and the temporalis muscle was pulled to expose the skull. A small window was created over the MCA by using an electric drill to thin the skull until the internal layer of the bone was fractured. The bone pieces were removed carefully, exposing the MCA (Fig. 2(a), (d)). The permanent occlusion of the MCA was induced by coagulation and a visual confirmation of blood perfusion was assessed (Fig. 2(e)). The skin incisions were closed with interrupted nylon sutures.

2.2.3. Photothrombotic stroke (PT stroke)

PT stroke was performed as described previously [19]. Mice were anesthetized with 1.5 % isoflurane in 30 % oxygen and 70 % nitrogen using a face mask and then placed in a stereotaxic frame. Body temperature was maintained at 37.0 ± 0.5 °C using a recirculating water heating pad. The skull was exposed by a dorsal midline incision, and a cold green light with a 2.5-mm opening light guide was positioned at 1.5 mm from the bregma. Mice received intraperitoneal injection of Rose Bengal (10 mg/mL in saline, 0.1 mg per gram of body weight). Five minutes later, the green light was turned on to induce cortical vessel occlusion by illumination through the intact skull for 15 min (Fig. 2(b)). Skin incisions were closed with interrupted nylon sutures or tissue adhesive (3 M, Vetbond, USA). An example of PT stroke at day 1 after injury is shown in Fig. 2(g).

2.3. Animal imaging procedure

The mouse brain imaging was performed with PAUSAT one day before, and one or three days after the PT or pMCAO stroke operation, respectively. PAUSAT imaging was entirely noninvasive, with the scalp and skull intact. To prepare the brain imaging, we used 5 % isoflurane for anesthesia induction, and 1–1.5 % isoflurane for anesthesia maintaining. The mouse scalp was shaved. A 100-microliter solution of microbubbles (VesselVue, SonoVol Inc., Durham, USA) with a concentration of 2.43×10^9 microbubbles/mL was injected retro-orbitally using a 27-gauge needle. The high microbubble concentration allowed a circulation time of $> \sim$10 min. The mice were then mounted in a supine position on a custom height-adjustable ramp. The body temperatures were regulated at 36.0 ± 1.0 °C with a heating pad and an infrared heating lamp. The heads were positioned just above the transparent membrane of the imaging window. A thin layer of room temperature water was added to the imaging window for acoustic coupling. The internal body temperatures of the mice were closely monitored during imaging via an anal thermocouple probe. A B-mode US scan was first performed at 16 MHz, which allowed for deeper penetration through intact skull. Two AA scans were performed with different focal depths by adjusting the height of the mounting ramp. The B-mode US scan took ~1 min, and the first AA scan was initiated 1–2 min post microbubble injection. The first AA scan focused at deeper brain vasculature while the second scan focused at cortical brain vasculature. The microbubble signal strength in deeper regions was lower than that in the superficial regions, but the microbubble concentration was lower in the second scan. Thus, the signal strength in both scans was similar. The two scans were later combined and normalized individually (Supplementary Fig. 1). Each AA frame was averaged 10 times per elevational position to increase signal-to-noise ratio and the elevational scanning step size was 0.2 mm over a 20 mm scanning range. Each AA scan took ~5 min. Two PACT scans were performed at 756 nm and 798 nm. The PACT scans were each averaged 10 frames per elevational position, with a scanning step size of 0.4 mm over a 20 mm range. Each PACT scan took ~1 min. Including transition time between modalities, a complete PAUSAT imaging sequence took ~20 min post-microbubble injection. The optical fluence of the laser pulses on the mouse scalp surface was ~10 mJ/cm^2 for both wavelengths.

2.4. Laser speckle contrast imaging (LSCI)

Cortical blood flow of the brain was measured using a full-field laser perfusion imager (RFLSI III, RWD, Life Science Co., Ltd.) as described previously [20]. A midline scalp incision was performed, and the skull was exposed. The imager was positioned above the skull and the following parameters were used: 2.5× magnification, exposure time 10 ms, continuous recording for 1 s, and image size 2048 × 2048 pixels (Fig. 2(c), (f), (h), (i)).

2.5. Infarct volume measurement

By TTC staining: Infarct volume was quantified using the 2,3,5-triphenyltetrazolium chloride (TTC) staining method. The mice were deeply anesthetized with isoflurane (5 % isoflurane in 30 % oxygen and 70 % nitrogen) and the brains were removed. Coronal Section (1 mm thick) were incubated with 2 % TTC for 15 min at room temperature and immediately fixed using 30 % formalin for at least 30 min. A macroscopic image of the coronal sections beside a metric ruler was acquired. The ruler reference was used to determine the pixel dimensions, and the infarct regions were manually segmented to calculate the infarct area. The segmented areas were then linearly interpolated to estimate the total stroke volume considering the thickness of the coronal sections.

By AA imaging: A similar procedure was followed to calculate the corresponding stroke volume using the AA data. The infarct region was segmented for each frame (0.2 mm thick) and the area was calculated. The segmented areas were then linearly interpolated to estimate the total stroke volume.

2.6. PAUSAT of the pMCAO and PT stroke models

Using our co-registered PAUSAT system, we were able to compare the blood perfusion and blood oxygenation before and 3 days after pMCAO stroke, and 1 day after PT stroke. The co-registered AA, B-mode US, and PACT images allow the identification of the stroke-impaired brain structures and functional regions more easily by providing complimentary information. The B-mode US image is particularly useful for identifying the structure of the brain, such as the skull and brain perimeter. Using the skull's structural information, we can create a spatial mask to accurately remove the signals originating from the scalp in the PACT images. The two PACT images were both low-pass filtered to reduce the effects of small displacement due to breathing motion, prior to the calculation of sO_2. The PAUSAT results were validated by TTC staining of the whole brain extracted after the imaging.

2.7. Measurement of oxygen saturation of hemoglobin (sO_2)

Oxygen saturation of hemoglobin was quantified by using two laser wavelengths at 756 nm and 798 nm. These two wavelengths are commonly used in photoacoustic studies of blood oxygenation for several reasons [21–23]. First, 756 nm is a local maximum of the ratio between HbR and HbO_2 optical absorption. Second, 798 nm is approximately an isosbestic point of optical absorption between HbR and HbO_2. Third, both wavelengths have relatively similar penetration depth in tissue, thus the impact due to wavelength-dependent fluence is minimized. Once the 756 nm and 798 nm images were acquired, we used a linear-model-based method to quantify relative concentration of HbO_2 (i.e., sO_2)[24]. We compensated for the optical fluence on the scalp surface but did not compensate for the wavelength-dependent optical attenuation inside the brain tissue. However, because statistical comparisons were performed between left and right hemispheres at

the same depth in the brain, the impact of wavelength-dependent optical attenuation on the sO_2 calculation was reduced. Relative changes in the calculated sO_2 were reported.

2.8. Statistical analysis

Blood oxygenation and blood perfusion analyses: Changes in blood oxygenation and blood perfusion between the left and right upper hemispheres of control, pMCAO, and PT mice were analyzed ($n = 3$ mice/group). Two regions-of-interest (ROIs) were defined for each mouse: the left upper hemisphere and the right upper hemisphere. For each ROI, blood oxygenation was measured by calculating the mean intensity of the pixels in the ROI, using the sO_2 images. Similarly, blood perfusion was measured by calculating the mean intensity of the pixels in the ROI, using the normalized AA images. For each mouse, the left ROI was symmetric with the right ROI, and therefore they contained the same number of pixels. These ROIs were individually adjusted to each mouse in order to avoid mismatches due to variations in brain size between mice. For both blood oxygenation and blood perfusion, the percent change from left to right ROI was calculated for each mouse group, and a one-sample t-test was performed to evaluate the statistical difference.

Infarct volume analysis: The stroke-infarct volume was calculated using TTC slices and AA data. The data were divided into pMCAO stroke mice and PT stroke mice ($n = 3$ mice/group). A paired t-test was performed to identify significant differences ($p < 0.05$) between the calculated infarct volume using TTC slices versus using AA data for both stoke model groups. Statistical data are presented as mean ± standard deviation.

The above-mentioned analyses were performed using MATLAB R2021b (The MathWorks Inc., Natick, MA).

3. Results

3.1. Image co-registration of the PAUSAT system

The dual-element wobbler transducer and the PA linear-array transducer of the PAUSAT system are rigidly mounted to the same motorized stage, thus knowledge of their relative distance enables automatic co-registration of PACT, US, and AA images. Note that the US and AA share the same wobbler transducer. We used a grid phantom made of thin copper wire (diameter: 10 μm) to accurately measure the distance between the PA linear-array transducer and the dual-element wobbler transducer (Fig. 3). The phantom was first imaged using the wobbler B-mode US at 35 MHz (Fig. 3(a)). The motorized stage was then moved until the PA linear-array transducer was approximately aligned with the copper wire grid phantom, and the translation distance was recorded. The phantom was then imaged using the linear-array transducer for PACT at 532 nm (Fig. 3(b)). The 3D US and the PA images were then co-registered in the axial, lateral, and elevational axes by rigid shifting (Fig. 3(c) (d) (e)). The measured distance between the wobbler and the linear array transducer is then recorded and used for the automatic image co-registration for all the other experiments.

3.2. Characterization of the PAUSAT system resolutions

We further quantified the spatial resolution of different imaging modes of PAUSAT. For PACT and B-mode US, copper wires (diameter:

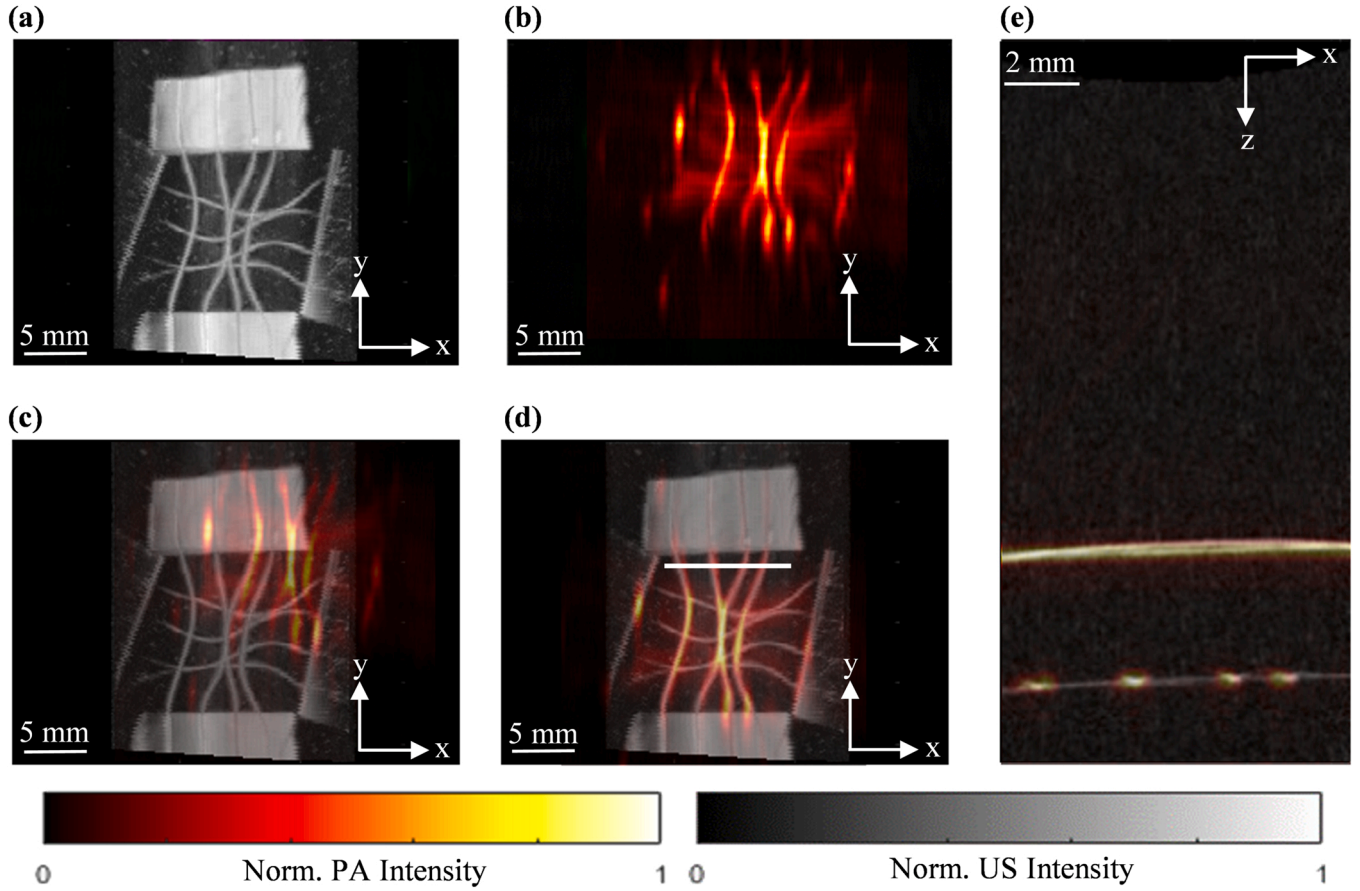

Fig. 3. Image co-registration of the PAUSAT system using a copper wire grid phantom. (a) B-mode US image projected along the axial axis. (b) PACT image projected along the axial axis. (c) Overlay of PACT and B-mode US images before alignment. (d) Overlay of PACT and B-mode US images after alignment along the lateral and elevational axis. (e) Overlay of PACT and B-mode US images after alignment along the axial axis at the x-y plane indicated by the white line in (d).

10 μm) were used to estimate line spread functions (LSFs) for the lateral and elevational axes and the point spread function (PSF) for the axial axis. For AA, a silicone tube (internal diameter: 200 μm) perfused with VesselVue MBs was used to estimate the LSF and PSF (Supplementary Fig. 2). The resolution is defined as the full width at half maximum (FWHM) of the PSF for all three dimensions. As shown in Table 1, all resolutions are sub-millimeter except for the elevational resolution of PACT, which is approximately 2 mm (note the significant blurring along the y-axis in Fig. 3(b)). The elevational resolution for PACT is mainly determined by the weak focusing of the acoustic lens [25]. The resolutions of different imaging modes are variously determined by the frequency, aperture size (~38 mm for the linear-array, ~10 mm for wobbler), focusing, and/or the transmission pulsewidth. Note that B-mode US resolution shown in Table 1 can vary with the transmission frequency and axial depth. We chose 35 MHz for the resolution measurement, which is close to the central frequency.

3.3. Quantitative analysis of the stroke-induced hemodynamic changes by PAUSAT

We were able to identify the stroke region of the pMCAO (Fig. 4) and PT (Fig. 5) stroke models using the PACT and AA images. The B-mode US images were used to provide the structural information of the skull (Fig. 4(a), Fig. 5(a)). The AA images were used to evaluate the blood perfusion change (Fig. 4(b), Fig. 5(b)). The PACT images were used to evaluate the blood oxygenation change (Fig. 4(c), (d), Fig. 5(c), (d)). For both AA and PACT images, the stroke-impaired regions can be clearly identified as the reduced blood perfusion and oxygenation, respectively, which were confirmed by the TTC-staining results (Figs. 4(e) and 5(e)).

The stroke-induced hemodynamic changes were quantitatively analyzed by comparing the PAUSAT measurements in the contralateral (intact) and ipsilateral (infarct) hemispheres of the brain (Fig. 6(a)). From the AA images, the blood perfusion in the ipsilateral hemisphere showed a 32 ± 11 % ($p = 0.042$, $n = 3$) and 29 ± 4 % ($p = 0.005$, $n = 3$) decrease, compared with that in the contralateral hemisphere for pMCAO and PT stroke models, respectively. By contrast, in the control mice, there was no significant difference in blood perfusion between the two hemispheres (2.4 ± 3.0 %; $p > 0.05$, $n = 3$ (Fig. 6(b)). These results have demonstrated that AA images can be used to identify the stroke region by quantifying blood perfusion decrease induced by ischemic stroke. Similarly, the PACT images showed a significant decrease in the blood oxygenation level in the peri-infarct region, in both pMCAO and PT stroke models, by 19 ± 7 % ($p = 0.046$, $n = 3$) and 14 ± 3 % ($p = 0.015$, $n = 3$), respectively (Fig. 6(b)). This contrasted with our control group, which did not show a significant difference in sO_2 between hemispheres (2.6 ± 5.4 %; $p > 0.05$, $n = 3$). The calculated sO_2 results of the healthy brain regions were consistent with previously published PAM studies [26–28]. However, we expect that at greater depths the accuracy of our calculation was lower.

Measuring the volume of brain tissue with little to no blood perfusion, or the infarct volume, is of particular interest in quantifying stroke-induced tissue damage. The infarct volume is traditionally estimated by segmenting and interpolating the stroke areas of the limited number of TTC slices of the extracted brain tissue [29,30], shown in Fig. 7. The TTC-based method does not allow longitudinal measurement of the infarct volume (Fig. 7(a)). By contrast, our AA imaging can clearly detect blood perfusion of the brain tissue in 3D, and thus the infarct volume can be estimated by measuring the no-perfusion volume inside the brain. A paired t-test comparing the stroke volume quantified using AA data and TTC staining for the pMCAO model and PT model showed no statistical difference. The AA-based method is more efficient than the TTC-based method and does not need to sacrifice the animals, allowing for longitudinal study.

Table 1
The spatial resolutions of different imaging modes of the PAUSAT system.

	PACT	B-mode US (35 MHz)	AA
Lateral (x)	0.45 mm	0.35 mm	0.42 mm
Axial (z)	0.35 mm	0.15 mm	0.36 mm
Elevational (y)	2.0 mm	0.38 mm	0.40 mm

4. Conclusion and discussion

In this work, we have reported using our recently-developed PAUSAT system that seamlessly integrates 3D PACT, B-mode US, and AA imaging to study ischemic stroke. PAUSAT can provide co-registered morphological and functional images of the mouse brain with complementary information. We demonstrated the ability of PAUSAT to longitudinally and non-invasively evaluate ischemic stroke via blood perfusion and blood oxygenation measurements. We confirmed previously reported results of decreased oxygenation in stroke-impaired regions of the brain as measured using PACT [31,32]. We also demonstrated, using two common ischemic stroke animal models, that AA can be used to reliably quantify infarct volume. Together, PAUSAT can be a powerful tool in future longitudinal studies of ischemic stroke treatments.

Pre-clinical studies of brain disorders could benefit from our co-registered PAUSAT technology. Since the majority of stroke patients do not receive reperfusion therapy, we used two common permanent stroke models in the current study. Most studies evaluating the progression of the stroke rely on post-mortem histological analysis [33–35], which requires a large number of animals per time-point studied due to the inter-animal variations. The three Rs principle emphasizes the "replacement, reduction, and refinement" of lab animals, recommending researchers to optimize experimental designs to reduce the number of animals required. The PAUSAT technology presented here allows the evaluation of the stroke in a non-invasive and longitudinal manner, and thus requires a much smaller number of animals needed to achieve the same statistical power.

In this proof-of-concept study, we evaluated two different models of permanent stroke. The most important characteristic of permanent stroke is the complete lack of blood perfusion within the injury site. This lack of blood supply (ischemia) leads to local hypoxia and tissue infarct. These physiological features manifest as decreased blood perfusion and blood oxygenation, allowing the stroke models to be observed by both AA and PACT in a completely non-invasive manner with both the scalp and skull intact. Although LSCI is widely used in stroke study [36,37] providing blood flow information without removing the skull, it cannot quantify the blood oxygenation and is restricted to evaluate the superficial infarct area. By contrast, the limitation of LSCI is easily overcome by the seamless integration of AA and PACT. Other stroke models, like the transient MCAO model, in which the blood perfusion of the brain tissue is blocked for a short period and subsequently restored, may also be evaluated by our technology. In this case, AA can provide information regarding the re-perfusion process and changes in the blood supply, and PACT can locate the area where the blood oxygenation has been mainly changed. It is also worth highlighting that PAUSAT is not limited to the study of stroke, but it also allows for evaluating disease progression and treatment effectiveness in other organs of the body. For example, most cancers are known to show increased density and tortuosity of blood vessels and decreased blood oxygenation [38,39]. Using PAUSAT, we can measure the changes in tumor volume, tortuosity and density of blood vessels, and blood oxygenation in cancerous tissues, and provide non-invasive and longitudinal preclinical studies of cancer therapies. Furthermore, when imaging soft-tissue tumors without the acoustic distortion by skull (e.g., breast cancer, liver cancer, prostate cancer), the image quality is often significantly improved over the brain studies with the acoustic distortions of the skull [40,41].

The image quality of our system can be improved by a few key design modifications. First, the ultrasound transducer used for the PACT is a linear-array transducer that has limited detection angle range relative to

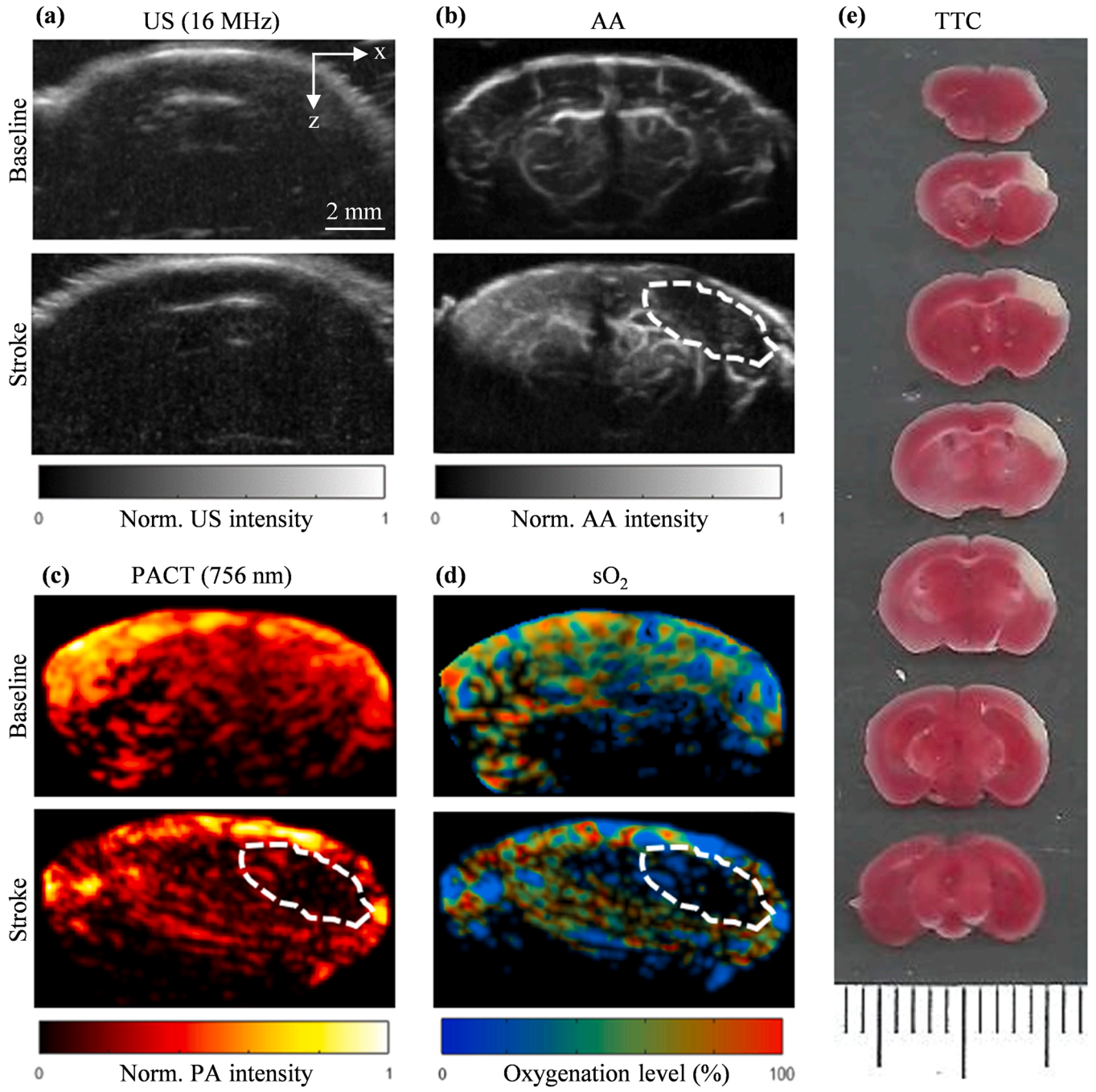

Fig. 4. Baseline and pMCAO stroke images of the mouse brain. (a) Baseline and post-stroke B-scan US coronal images. (b) Baseline and post-stroke AA coronal image (dashed outline shows stroke region). (c) PACT coronal image at 756 nm. (d) sO_2 coronal image calculated using the 756 nm and 798 nm PA data. (e) TTC stained 1 mm-thick coronal slices of mouse brain after PAUSAT imaging (white areas indicate stroke infarct).

the target. This introduces the limited-view reconstruction artifacts for our PACT [42]. Although many efforts have been made to mitigate the effects of the limited-view problem via modifications to the reconstruction algorithm [43–45], the most effective solution is to improve the hardware. This includes, for example, using a half-ring-array transducer rather than a linear-array transducer [46–48]. However, the half-ring-array system presents different limitations, such as the animal positioning and acoustic coupling. Another alternative is rotating the linear-array transducer to provide a larger viewing angle range, which, however, will slow down the imaging [49]. In addition to acoustic challenges, there are also optical challenges. The light delivery is currently limited to the top of the head. Using 360-degree light illumination would allow for the excitation of deeper tissue [50]. Alternatively, internal illumination has proved useful for improving photoacoustic image quality in vivo [51–53]. The accuracy of the sO_2 calculation is also limited due to wavelength-dependent fluence attenuation of the excitation light [54]. A Monte Carlo simulation can be used to compensate for wavelength-dependent fluence, although it results in a greater computational expense [55,56].

The relatively long time required for completing the whole imaging process also degrades the quality of information attained in live animal experiments. This includes the time delay between tuning wavelengths for PACT and between the transducer repositioning between AA and PACT image acquisitions. Since PACT and AA scans are performed

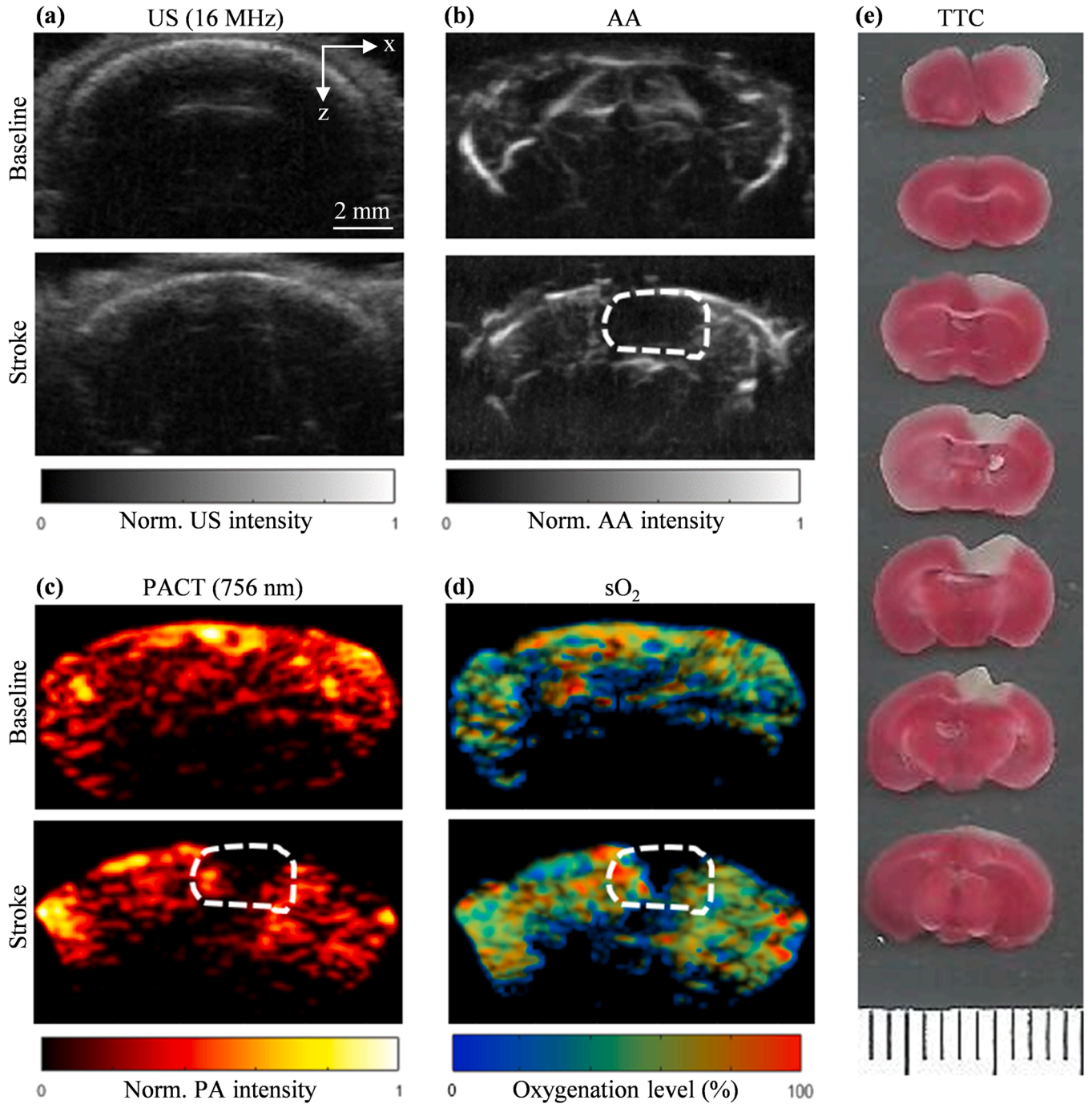

Fig. 5. Baseline and PT stroke images of the mouse brain. (a) Baseline and post-stroke B-scan US coronal images. (b) Baseline and post-stroke AA coronal image (dashed outline shows stroke region). (c) 756 nm PA coronal image. (d) sO_2 coronal image calculated using the 756 nm and 798 nm PA data. (e) TTC stained 1 mm-thick coronal slices of mouse brain after PAUSAT imaging (white areas indicate stroke infarct).

separately, a significant amount of time is spent on changing the imaging mode. The time delay between PACT and AA scans leads to variance in local blood flow and body position (mainly due to breathing). The same problem exists for multi-wavelength PACT scans since these images are also acquired separately. In our next step, the system will include a stereotaxic frame to reduce head motion, acquire multiple wavelengths for a single PA scan, and perform the AA scan concurrently with PA, all within tens of seconds. To do so, the PACT system may also use the same wobbler transducer for signal detection, with excitation laser light delivered through an optical fiber mounted on the wobbler. The dual-element wobbler transducer has a fixed focus and is mounted on a motorized stage that moves along the lateral and elevational axes. In our experiments, we designed a 3D-printed mouse ramp attached to a manual translation stage to adjust the focal depth inside the mouse brain. The manual translation may cause an orientation change of the mouse head, leading to misalignment of the images acquired at multiple focal depths. This issue can be addressed by adding a motorized stage to translate the wobbler transducer along the axial axis with high precision.

In conclusion, our results have demonstrated that the co-registered PACT, US, and AA imaging by our PAUSAT system allows simultaneous monitoring of morphological and functional changes on small-animal stroke models. Our technology may become a valuable tool for the developing therapeutic strategies in neurological diseases and

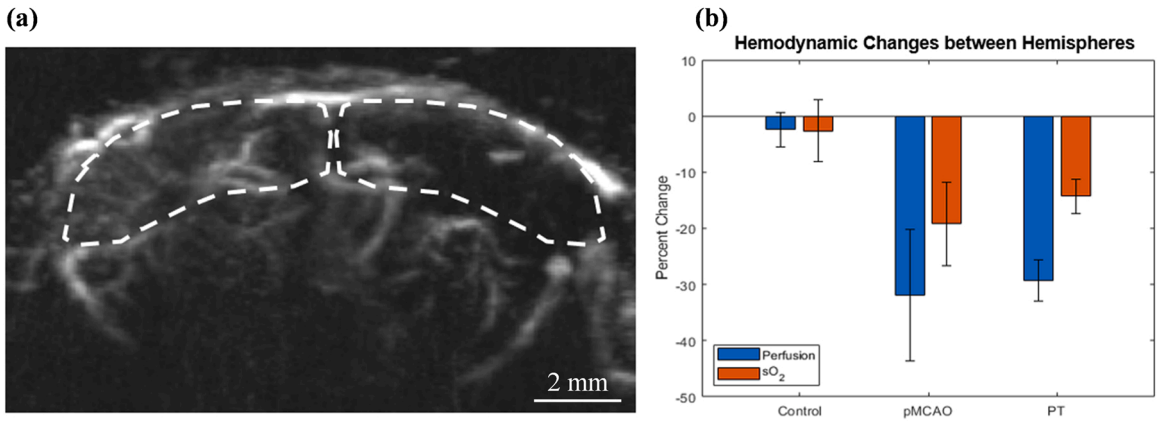

Fig. 6. Comparison of blood perfusion and oxygenation of the stroke-impaired hemisphere with that of the healthy hemisphere. (a) Example regions of interest (dotted line) marked on an AA image of a pMCAO-stroke mouse. (b) Percentage change in blood perfusion (calculated as normalized AA intensity) and sO_2 between the stroke-impaired and healthy hemispheres of the control mice, pMCAO stroke mice, and PT stroke mice (n = 3/group).

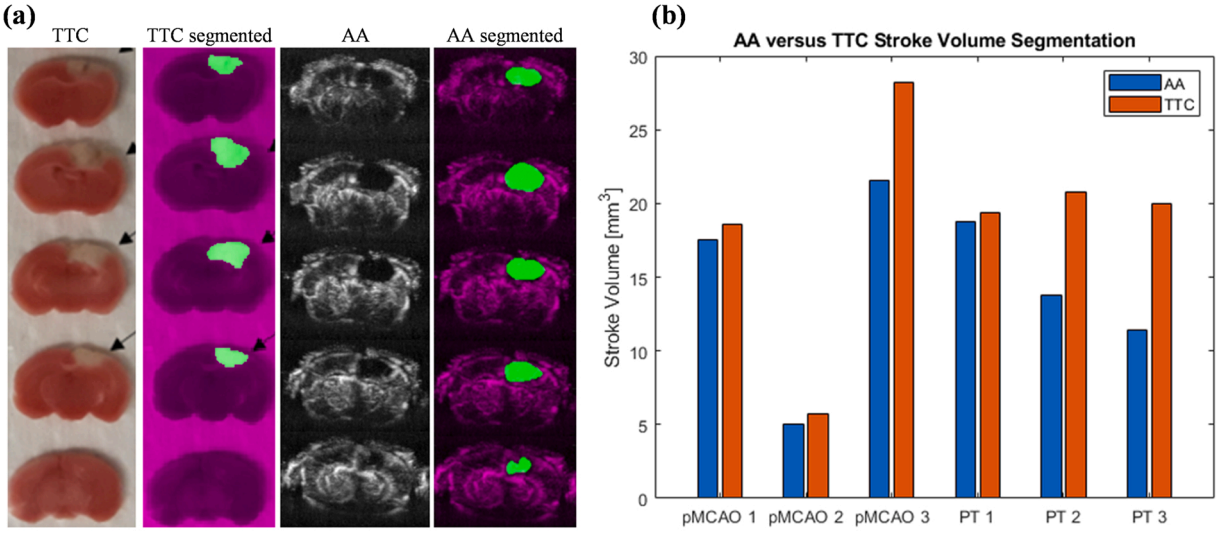

Fig. 7. Quantification of stroke-induced infarct volume. (a) Example TTC slices (PT stroke), segmented TTC slices, AA images, and segmented AA images at corresponding coronal locations. (b) Direct comparison of infarct volumes as measured from segmented TTC slices and AA volume on pMCAO mice (n = 3) and PT mice (n = 3). A paired t-test comparing the TTC versus AA results showed no statistical difference for either stroke model ($p > 0.05$).

cancers beyond stroke.

Declaration of Competing Interest

The authors declare no conflict of interest in this work.

Data availability

Data will be made available on request.

Acknowledgments

The authors would like to acknowledge the engineering team at SonoVol Inc. for their technical support. This work was partially sponsored by American Heart Association Collaborative Sciences Award (18CSA34080277), to J. Yao and W. Yang; The United States National Institutes of Health (NIH) grants R21EB027981, R21 EB027304, RF1 NS115581 (BRAIN Initiative), R01 NS111039, R01 EB028143; The United States National Science Foundation (NSF) CAREER award 2144788; and Chan Zuckerberg Initiative Grant (2020–226178), to J. Yao.

Appendix A. Supporting information

Supplementary data associated with this article can be found in the online version at doi:10.1016/j.pacs.2022.100444.

References

[1] K. Hochrainer, W. Yang, Stroke proteomics: from discovery to diagnostic and therapeutic applications, Circ. Res. 130 (8) (2022) 1145–1166.
[2] S.S. Virani, et al., Heart disease and stroke statistics—2021 update: a report from the American Heart Association, Circulation 143 (8) (2021) e254–e743.
[3] J. Xu, S. Murphy, K. Kochanek, B. Bastian, and E. Arias, "Deaths: Final data for 2013 National vital statistics reports; vol 64 no 2," Hyattsville, MD: National Center for Health Statistics, 2016.
[4] H.K. Siddiqi, P. Libby, P.M. Ridker, COVID-19 – a vascular disease, Trends Cardiovasc. Med. 31 (1) (2021) 1–5, https://doi.org/10.1016/j.tcm.2020.10.005.
[5] K. South, L. McCulloch, B.W. McColl, M.S. Elkind, S.M. Allan, C.J. Smith, Preceding infection and risk of stroke: an old concept revived by the COVID-19 pandemic, Int. J. Stroke 15 (7) (2020) 722–732.
[6] J.D. Spence, et al., Mechanisms of stroke in COVID-19, Cerebrovasc. Dis. 49 (4) (2020) 451–458.
[7] P. Beard, Biomedical photoacoustic imaging, Interface Focus 1 (4) (2011) 602–631.
[8] M. Xu, L.V. Wang, Photoacoustic imaging in biomedicine, Rev. Sci. Instrum. 77 (4) (2006), 041101.
[9] S.L. Jacques, Optical properties of biological tissues: a review, Phys. Med. Biol. 58 (11) (2013) R37.

[10] W. Lin, W.J. Powers, Oxygen metabolism in acute ischemic stroke, J. Cereb. Blood Flow. Metab. 38 (9) (2018) 1481–1499.
[11] H. An, et al., Imaging oxygen metabolism in acute stroke using MRI, Curr. Radiol. Rep. 2 (3) (2014) 1–10.
[12] L.V. Wang, J. Yao, A practical guide to photoacoustic tomography in the life sciences, Nat. Methods 13 (8) (2016) 627–638.
[13] R.C. Gessner, C.B. Frederick, F.S. Foster, P.A. Dayton, Acoustic angiography: a new imaging modality for assessing microvasculature architecture, Int. J. Biomed. Imaging 2013 (2013).
[14] P.A. Dayton, J.J. Rychak, Molecular ultrasound imaging using microbubble contrast agents, Front. Biosci. -Landmark 12 (13) (2007) 5124–5142.
[15] T.J. Czernuszewicz, et al., A new preclinical ultrasound platform for widefield 3D imaging of rodents, Rev. Sci. Instrum. 89 (7) (2018), 075107.
[16] M. Li, et al., Three-dimensional deep-tissue functional and molecular imaging by integrated photoacoustic, ultrasound, and angiographic tomography (PAUSAT), IEEE Trans. Med. Imaging (2022).
[17] A. Lasso, T. Heffter, A. Rankin, C. Pinter, T. Ungi, G. Fichtinger, PLUS: open-source toolkit for ultrasound-guided intervention systems, IEEE Trans. Biomed. Eng. 61 (10) (2014) 2527–2537.
[18] X. Li, et al., Single-cell transcriptomic analysis of the immune cell landscape in the aged mouse brain after ischemic stroke, J. Neuroinflamm. 19 (1) (2022) 83, https://doi.org/10.1186/s12974-022-02447-5.
[19] Z. Wang, et al., Increasing O-GlcNAcylation is neuroprotective in young and aged brains after ischemic stroke, Exp. Neurol. 339 (2021), 113646.
[20] W. Wang, et al., Development and evaluation of a novel mouse model of asphyxial cardiac arrest revealed severely impaired lymphopoiesis after resuscitation, J. Am. Heart Assoc. 10 (11) (2021), e019142.
[21] E. Fakhrejahani, et al., Clinical report on the first prototype of a photoacoustic tomography system with dual illumination for breast cancer imaging, PLOS One 10 (10) (2015), e0139113.
[22] Y. Matsumoto, et al., Visualising peripheral arterioles and venules through high-resolution and large-area photoacoustic imaging, Sci. Rep. 8 (1) (2018) 1–11.
[23] J. Menke, Photoacoustic breast tomography prototypes with reported human applications, Eur. Radiol. 25 (8) (2015) 2205–2213.
[24] M. Li, Y. Tang, J. Yao, Photoacoustic tomography of blood oxygenation: a mini review, Photoacoustics 10 (2018) 65–73.
[25] H. Zhang, et al., Deep-E: a fully-dense neural network for improving the elevation resolution in linear-array-based photoacoustic tomography, IEEE Trans. Med. Imaging 41 (5) (2021) 1279–1288.
[26] R. Cao, et al., Functional and oxygen-metabolic photoacoustic microscopy of the awake mouse brain, Neuroimage 150 (2017) 77–87.
[27] X. Zhu, et al., Real-time whole-brain imaging of hemodynamics and oxygenation at micro-vessel resolution with ultrafast wide-field photoacoustic microscopy, Light.: Sci. Appl. 11 (1) (2022) 1–15.
[28] T. Wang, et al., Multiparametric photoacoustic microscopy of the mouse brain with 300-kHz A-line rate, Neurophotonics 3 (4) (2016), 045006.
[29] J. Iwanami, et al., Pretreatment with eplerenone reduces stroke volume in mouse middle cerebral artery occlusion model, Eur. J. Pharmacol. 566 (1–3) (2007) 153–159.
[30] H.K. Lee, S.J. Widmayer, M.-N. Huang, D.L. Aylor, D.A. Marchuk, Novel neuroprotective loci modulating ischemic stroke volume in wild-derived inbred mouse strains, Genetics 213 (3) (2019) 1079–1092.
[31] J. Lv, et al., In vivo photoacoustic imaging dynamically monitors the structural and functional changes of ischemic stroke at a very early stage, Theranostics 10 (2) (2020) 816.
[32] J. Yao, L.V. Wang, Photoacoustic brain imaging: from microscopic to macroscopic scales, Neurophotonics 1 (1) (2014), 011003.
[33] S.T. Carmichael, Rodent models of focal stroke: size, mechanism, and purpose, NeuroRx 2 (3) (2005) 396–409.
[34] E. Esposito, et al., Potential circadian effects on translational failure for neuroprotection, Nature 582 (7812) (2020) 395–398.
[35] Z. Wang, et al., Shikonin protects mouse brain against cerebral ischemia/reperfusion injury through its antioxidant activity, Eur. J. Pharmacol. 643 (2–3) (2010) 211–217.
[36] G.A. Armitage, K.G. Todd, A. Shuaib, I.R. Winship, Laser speckle contrast imaging of collateral blood flow during acute ischemic stroke, J. Cereb. Blood Flow. Metab. 30 (8) (2010) 1432–1436.
[37] A.K. Dunn, Laser speckle contrast imaging of cerebral blood flow, Ann. Biomed. Eng. 40 (2) (2012) 367–377.
[38] C.-Y. Li, et al., Initial stages of tumor cell-induced angiogenesis: evaluation via skin window chambers in rodent models, J. Natl. Cancer Inst. 92 (2) (2000) 143–147.
[39] B. Muz, P. de la Puente, F. Azab, A.K. Azab, The role of hypoxia in cancer progression, angiogenesis, metastasis, and resistance to therapy, Hypoxia 3 (2015) 83.
[40] B. Liang, et al., Impacts of the murine skull on high-frequency transcranial photoacoustic brain imaging, J. Biophotonics 12 (7) (2019), e201800466.
[41] B. Liang, S. Wang, F. Shen, Q.H. Liu, Y. Gong, J. Yao, Acoustic impact of the human skull on transcranial photoacoustic imaging, Biomed. Opt. Express 12 (3) (2021) 1512–1528.
[42] Y. Xu, L.V. Wang, G. Ambartsoumian, P. Kuchment, Reconstructions in limited-view thermoacoustic tomography, Med. Phys. 31 (4) (2004) 724–733.
[43] X. Ma, et al., Multiple delay and sum with enveloping beamforming algorithm for photoacoustic imaging, IEEE Trans. Med. Imaging 39 (6) (2019) 1812–1821.
[44] G. Paltauf, R. Nuster, M. Haltmeier, P. Burgholzer, Experimental evaluation of reconstruction algorithms for limited view photoacoustic tomography with line detectors, Inverse Probl. 23 (6) (2007) S81.
[45] T. Vu, M. Li, H. Humayun, Y. Zhou, J. Yao, A generative adversarial network for artifact removal in photoacoustic computed tomography with a linear-array transducer, Exp. Biol. Med. 245 (7) (2020) 597–605.
[46] T. Chen, et al., Dedicated photoacoustic imaging instrument for human periphery blood vessels: a new paradigm for understanding the vascular health, IEEE Trans. Biomed. Eng. 69 (3) (2021) 1093–1100.
[47] J. Xia, L.V. Wang, Small-animal whole-body photoacoustic tomography: a review, IEEE Trans. Biomed. Eng. 61 (5) (2013) 1380–1389.
[48] Y. Zhang, L. Wang, Video-rate ring-array ultrasound and photoacoustic tomography, IEEE Trans. Med. Imaging 39 (12) (2020) 4369–4375.
[49] P. Zhang, et al., High-resolution deep functional imaging of the whole mouse brain by photoacoustic computed tomography in vivo, J. Biophotonics 11 (1) (2018), e201700024.
[50] J. Yao, K.I. Maslov, E.R. Puckett, K.J. Rowland, B.W. Warner, L.V. Wang, Double-illumination photoacoustic microscopy, Opt. Lett. 37 (4) (2012) 659–661.
[51] M. Li, B. Lan, W. Liu, J. Xia, J. Yao, Internal-illumination photoacoustic computed tomography, J. Biomed. Opt. 23 (3) (2018), 030506.
[52] M. Li, et al., Internal-illumination photoacoustic tomography enhanced by a graded-scattering fiber diffuser, IEEE Trans. Med. Imaging 40 (1) (2020) 346–356.
[53] L. Lin, J. Xia, T.T. Wong, L. Li, L.V. Wang, In vivo deep brain imaging of rats using oral-cavity illuminated photoacoustic computed tomography, J. Biomed. Opt. 20 (1) (2015), 016019.
[54] B. Cox, J. Laufer, P. Beard, The challenges for quantitative photoacoustic imaging, in: Photons Plus Ultrasound: Imaging and Sensing, vol. 7177, SPIE,, 2009, pp. 294–302.
[55] Y. Tang, J. Yao, 3D Monte Carlo simulation of light distribution in mouse brain in quantitative photoacoustic computed tomography, Quant. Imaging Med. Surg. 11 (3) (2021) 1046.
[56] L. Wang, S.L. Jacques, L. Zheng, MCML—Monte Carlo modeling of light transport in multi-layered tissues, Comput. Methods Prog. Biomed. 47 (2) (1995) 131–146.

Luca Menozzi received his B.S. in Biomedical Engineering (BME) from the joint BME program at UNC Chapel Hill and North Carolina State University, along with a B.A. in Mathematics from UNC Chapel Hill. He is currently a Ph.D. student at the Department of Biomedical Engineering at Duke University. His research interests include photoacoustic tomography and acoustic angiography applied to ischemic stroke research.

Ángela del Águila, Ph.D. is a postdoctoral researcher in the Department of Anesthesiology at Duke University. She obtained a degree in Chemistry from the University of Almeria (2011, Almería, Spain). She obtained her Master's degree (2013) and Ph.D. degree (2017) in Biochemistry, Molecular Biology and Biomedicine from the University Complutense of Madrid (Spain). Currently, her work is focused on the immune system response after ischemic stroke and cardiac arrest.

Tri Vu received his bachelor's degree in Biomedical Engineering from State University of New York at Buffalo. He is currently a Ph.D. candidate at the Department of Biomedical Engineering at Duke University. His research interests are high-speed small-animal photoacoustic imaging systems and photoacoustic image enhancement using deep learning.

Chenshuo Ma received her B.S. (2011) degree in Mechanical Engineering, and M.S. (2014) degree in Material Engineering from Kunming University of Science and Technology (Yunan, China), and her Ph.D. (2018) degree in Biomedical Engineering from Macquire University (Sydney, Australia). She is currently working as a postdoc research associate at Duke University, focused on photoacoustic tomography imaging.

Wei Yang is an associate professor in the Department of Anesthesiology at Duke University Medical Center. He received a B.S. degree from Wuhan University (China), a M.S. degree from Institute of Microbiology (Chinese Academy of Science), and a Ph.D. degree from University of Rostock (Germany). His current research interest is centered on ischemia/reperfusion injury after ischemic stroke and cardiac arrest.

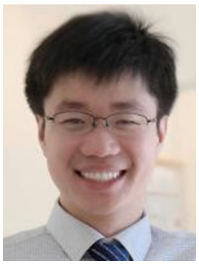

Prof. Dr. Junjie Yao is currently Assistant Professor at the Department of Biomedical Engineering at Duke University. Dr. Yao received his B.S. (2006) and M.S. (2008) degrees in Biomedical Engineering from Tsinghua University (Beijing, China), and his Ph.D. degree in Biomedical Engineering at Washington University in St. Louis in 2013. More information about Dr. Yao's research at http://photoacoustics.pratt.duke.edu/